Spin dynamics simulations of two-dimensional clusters with Heisenberg and dipole–dipole interactions

Spin dynamics simulations of two-dimensional clusters with Heisenberg and dipole–dipole interactions

Ph Depondt[1] **and F G Mertens**[2]

[1] Institut des NanoSciences de Paris, UMR CNRS 7588, Université Pierre et Marie Curie-Paris 6, F-75252 Paris Cedex 05, France
[2] Physikalisches Institut, Universität Bayreuth, D-95440 Bayreuth, Germany

E-mail: depondt@insp.jussieu.fr and franz.mertens@uni-bayreuth.de

Abstract
Spin dynamics with the Landau–Lifshitz equation has provided topics for a wealth of research endeavors. We introduce here a numerical integration method which explicitly uses the precession motion of a spin about the local field, thus intrinsically conserving spin lengths, and therefore allowing for relatively quick results for a large number of situations with varying temperatures and couplings. This method is applied to the effect of long-range dipole–dipole interactions in two-dimensional clusters of spins with nearest-neighbor XY-Heisenberg exchange interactions on a square lattice at finite temperature. The structures thus obtained are analyzed through orientational correlations functions. Magnon dispersion curves, different from those of the standard Heisenberg model, are obtained and discussed. The number of vortices in the system is discussed as a function of temperature and typical examples of vortex dynamics are shown.

(Some figures in this article are in colour only in the electronic version)

1. Introduction

Quasi-two-dimensional magnets of nanometric size, for instance deposited on a substrate, or layered compounds with negligible interlayer interactions, are of interest for quite a number of applications such as high-density data storage. Technical advances in producing such objects arise steadily (e.g. [1, 2]) and experiments are now apt to provide reliable data for such small systems (e.g. [3–13])

From a theoretical point of view, the dynamics of these materials is of great interest as it is strongly nonlinear and therefore unlikely to be easily addressed by analytical methods. Nonlinear coherent excitations, namely vortices and anti-vortices, can move around the sample and interact [14]. The XY-Heisenberg model, which includes nearest-neighbor spin–spin interactions, is well known as it yields a Kosterlitz–Thouless phase transition in which vortex–anti-vortex pairs break up above a critical temperature T_c. However, the spin–spin interactions are quite often not limited to such nearest-neighbor contributions but should also include long-range ($\propto 1/r^3$) dipolar interactions. This involves, of course, larger computational efforts but, for instance, Monte Carlo simulations [15] have shown spontaneous structuration of the spin orientations. A number of effects caused by dipolar interactions in systems with periodic boundary conditions are reviewed in [16]. Spin dynamics, because one has to add contributions from over the whole sample for many integration steps and because temperature must also be introduced, is computationally demanding but, by using efficient computational methods, one can hope to obtain not only new structures but also the associated dynamics [17, 18].

Our purpose is to introduce our methods for numerical integration of the Landau–Lifshitz classical spin dynamics equations using the Rodrigues rotation matrix [21] at finite temperature (section 2) and to validate these methods (section 3) by comparing with literature results our own results on the XY-Heisenberg model on a square lattice. In section 4, we include dipolar interactions. Their overall effect on structure, specifically correlation functions and elastic scattering functions, are shown and discussed. Computation

of dispersion curves yields the dynamics at a microscopic level. We also show thermal activation of vortices and their dynamics.

2. Model and numerical resolution

2.1. Ingredients of the model

We solve the Landau–Lifshitz equations for a finite square sample with a square lattice in the Heisenberg model and add long-range dipole–dipole interactions. The Landau–Lifshitz equations of motion are

$$\dot{\mathbf{s}}_i = -\mathbf{s}_i \times \mathbf{H}_i, \qquad \forall i \in [1, n] \tag{1}$$

where $\mathbf{s}_i$ stands for spin i with the constraint that the lengths of all spins remain constant:

$$|\mathbf{s}_i| = 1, \qquad \forall i, \, \forall t. \tag{2}$$

This 'constraint' is intrinsic to equation (1) so it is not really a constraint in the mathematical sense: however, a numerical integration scheme may very well not meet this requirement.

The local field $\mathbf{H}_i$ on spin $\mathbf{s}_i$ is

$$\mathbf{H}_i = - \sum_{\substack{j \\ \text{neighbour}(i)}} \mathbf{J}\mathbf{s}_j + d \sum_{\substack{j \\ (j \neq i)}} \left(\mathbf{s}_j - 3\frac{\mathbf{s}_j \cdot \mathbf{r}_{ij}}{|\mathbf{r}_{ij}|^2}\mathbf{r}_{ij} \right) \frac{1}{|\mathbf{r}_{ij}|^3} \tag{3}$$

where the first term on the right-hand side is the nearest-neighbor Heisenberg interaction with

$$\mathbf{J} = \begin{pmatrix} J_x & 0 & 0 \\ 0 & J_y & 0 \\ 0 & 0 & J_z \end{pmatrix}$$

and with $J_x = J_y = 1$. The out-of-plane coefficient J_z can be set at will: in this paper $J_z = 0$, i.e. we consider a Heisenberg-XY model that yields the well-known Kosterlitz–Thouless phase transition [19, 20]: in its static version, this model does not allow spins to have a component normal to the plane, but since the dynamics is simulated here, the s_z component of the spins is needed to let the motions fully develop. It should be noted that, despite the possibility for the spins to point out of the plane, this is a strictly single-layer system, not a 3D model in the limit of vanishing thickness.

The second term on the right-hand side of equation (3) is the dipole–dipole interaction, the strength of which is determined by d, and $\mathbf{r}_{ij} = \mathbf{r}_j - \mathbf{r}_i$, $\mathbf{r}_i$ being the position of spin i.

2.2. Numerical integration of the precession motion

Quite a number of methods can be used to solve the set of equations (1): established procedures are described in, for example, [17]. Since we deviate from the standard, we go back to elementary considerations: the explicit Euler integration scheme yields, for a time integration step δt:

$$\mathbf{s}_i(t + \delta t) = \mathbf{s}_i(t) + \dot{\mathbf{s}}_i(t)\delta t.$$

However

$$|\mathbf{s}_i(t + \delta t)|^2 = |\mathbf{s}_i(t) + \dot{\mathbf{s}}_i(t)\,\delta t|^2$$
$$= |\mathbf{s}_i(t)|^2 + 2\mathbf{s}_i(t) \cdot \dot{\mathbf{s}}_i(t)\,\delta t + |\dot{\mathbf{s}}_i(t)\delta t|^2$$
$$= |\mathbf{s}_i(t)|^2 + |\dot{\mathbf{s}}_i(t)\delta t|^2$$

results in a systematic and unphysical increase of $|\mathbf{s}_i(t)|$ with time. This can be addressed by rescaling $\mathbf{s}_i(t)$ at every step, a rather unsatisfactory procedure, however. The fourth-order Runge–Kutta integration scheme does four estimates of the derivatives, but some easy, albeit dull, calculations show that, although better than the Euler scheme, it also yields a systematic drift of $|\mathbf{s}_i(t)|^2$.

The alternative is to avoid blindfolded integration of the equations of motion by noting that the instantaneous motion of a spin is a precession about the instantaneous local field $\mathbf{H}_i(t)$. This, as pointed out in [22] where similar procedures are used, has the additional advantage that it does not require the precession angle to be small, but only for $\mathbf{H}_i$ to be slowly varying: should the local field remain constant with time, the time step δt could be chosen arbitrarily large. The time step thus depends on the characteristic time for the local field fluctuations. The precession can be explicitly carried out using the Rodrigues equation (see, for instance, [21]) that allows us to compute the rotation of a vector about another arbitrary vector:

$$\mathbf{s}_i(t + \delta t) = \mathbf{R}_i(t)\mathbf{s}_i(t) \tag{4}$$

where the rotation matrix is

$$\mathbf{R}_i(t) =$$
$$\begin{pmatrix} h_x^2 u + \cos \omega & h_x h_y u - h_z \sin \omega & h_x h_z u + h_y \sin \omega \\ h_x h_y u + h_z \sin \omega & h_y^2 u + \cos \omega & h_y h_z u - h_x \sin \omega \\ h_x h_z u - h_y \sin \omega & h_y h_z u + h_x \sin \omega & h_z^2 u + \cos \omega \end{pmatrix}$$

with $u = 1 - \cos \omega$ and h_x, h_y, h_z are the coordinates of the unit vector $\mathbf{h} = \mathbf{H}_i/|\mathbf{H}_i|$ which is parallel to the local field and the precession angle $\omega = |\mathbf{H}_i|\delta t$. The spin length is thus intrinsically conserved to numerical precision, as it should following equation (1). Reference [22] implements, as being more efficient, quaternions instead of a full rotation matrix, since a quaternion has only four components instead of nine: however, in our problem, since most of the computation time is taken by the dipolar interactions, the improvement should be marginal.

However, straightforward integration via equation (4) proves unreliable or would require unreasonably short time steps. An integration method inspired by the so-called 'improved Euler method' (or 'Heun's method' for ordinary differential equations, similar to a second-order Runge–Kutta method, based on an estimate of the derivatives at both ends of the integration step) is known to be efficient for multiplicative noise problems [17] and allows much better integration at the cost of two field computations per time step instead of one. We first compute as before a 'predicted' set of spins at time $t + \delta t$:

$$\mathbf{s}_i^p(t + \delta t) = \mathbf{R}_i(t)\mathbf{s}_i(t).$$

These predicted spins yield a new 'predicted' field estimate $\mathbf{H}_i^p(\{\mathbf{s}_j^p(t + \delta t)\})$ at the end of the time step $t + \delta t$. The 'corrected' field used to compute the corrected rotation matrix

$\mathbf{R}_i^c(t + \frac{\delta t}{2})$ estimated in the middle of the integration step is now the average of the fields at both ends of the integration step:

$$\mathbf{H}_i^c\left(t + \frac{\delta t}{2}\right) = \frac{\mathbf{H}_i(t) + \mathbf{H}_i^p(t + \delta t)}{2}$$

and

$$\mathbf{s}_i(t + \delta t) = \mathbf{R}_i^c\left(t + \frac{\delta t}{2}\right)\mathbf{s}_i(t).$$

We may now expect both quick and stable integration of equation (1).

2.3. Dipole–dipole interaction

The most computationally demanding part in such simulations is the dipole–dipole interaction term in equation (3). For small samples, it can be done by direct summation, but using the convolution theorem and fast Fourier transforms [17] greatly improves speed. In the case of a 2D square lattice, the position of spin i is $\mathbf{r}_i = (k_i a, \ell_i a)$, where a is the lattice constant and the dipolar field on spin i

$$\mathbf{H}_i^{dip} = d \sum_{\substack{j \\ (j \neq i)}} \left(\mathbf{s}_j - 3a\frac{s_{xj}(k_j - k_i) + s_{yj}(\ell_j - \ell_i)}{|\mathbf{r}_{ij}|^2}\mathbf{r}_{ij}\right)\frac{1}{|\mathbf{r}_{ij}|^3}$$

where $|\mathbf{r}_{ij}| = a\sqrt{(k_j - k_i)^2 + (\ell_j - \ell_i)^2}$. This can be seen as the convolution of $\mathbf{s}_i$ (or equivalently $\mathbf{s}_{k\ell}$) with the following matrix:

$$\mathbf{D}_{k\ell} = \frac{d}{a^3(k^2 + \ell^2)^{\frac{3}{2}}}\begin{pmatrix} 1 - 3\frac{k^2}{k^2+\ell^2} & -3\frac{k\ell}{k^2+\ell^2} & 0 \\ -3\frac{k\ell}{k^2+\ell^2} & 1 - 3\frac{\ell^2}{k^2+\ell^2} & 0 \\ 0 & 0 & 1 \end{pmatrix}.$$

This matrix and its two-dimensional Fourier transform can be computed beforehand.

The convolution itself is straightforward using FFTs and zero padding for a finite sample [24]: it is noteworthy that, since the spin distribution is discrete, the numerical discrete Fourier transform introduces no additional approximation.

2.4. Temperature control

We use Langevin dynamics to introduce temperature, following [23] and [14] which are analogous. The Langevin 'force' appears as a random or thermal field $\mathbf{H}_i^{th}$ with normal distribution, zero mean and variance

$$\langle (\mathbf{H}_i^{th})^2 \rangle = 2\alpha k_B T \tag{5}$$

where α is a damping coefficient, k_B is Boltzmann's constant (taken to be 1 in reduced units) and T is the temperature. The thermal field is added to $\mathbf{H}_i$ because spin $\mathbf{s}_i$ 'feels' the thermal noise only via the local field. The equations of motion (1) are thus modified:

$$\dot{\mathbf{s}}_i = -\frac{\mathbf{s}_i \times \mathbf{H}_i' + \alpha \mathbf{s}_i \times (\mathbf{s}_i \times \mathbf{H}_i')}{1 + \alpha^2} \tag{6}$$

with

$$\mathbf{H}_i' = \mathbf{H}_i + \mathbf{H}_i^{th}.$$

This is easily adapted to the Landau–Lifshitz equation in the Rodrigues formulation, as (6) can be rewritten as

$$\dot{\mathbf{s}}_i = -\mathbf{s}_i \times \mathbf{H}_i^{eff} \tag{7}$$

with

$$\mathbf{H}_i^{eff} = \frac{\mathbf{H}_i' + \alpha \mathbf{s}_i \times \mathbf{H}_i'}{1 + \alpha^2}.$$

The damping parameter α controls the speed at which the system relaxes towards equilibrium after a temperature change but, if chosen small enough, should have no other effect.

2.5. Technical details

The practical implementation of the above methods requires some care, as there is a potential contradiction between an integration scheme which is meant mainly for a slowly varying local field and the thermal field which must change randomly for every integration step. This could lead one to believe that the benefit of the slow variations is thus lost so that the only advantage would remain in the intrinsic conservation of spin lengths. This, however, is misleading: the time step δt is determined by the dynamics of the system, not thermal noise; first, the time step is determined, then only it must be explicitly included in the way the random field is generated, not the other way around. Namely, we use the standard Box–Muller method (e.g. [24]) for random numbers with Gaussian distribution and unit deviation. The numbers thus obtained should be multiplied by the standard deviation $\sqrt{2\alpha k_B T}$ for the thermal field values (equation (5)), but time discretization must be taken into account. Indeed, a given set of random numbers at time t will 'last' for a time step δt; since their standard deviation is one, they must be multiplied by a factor γ and

$$\langle (\mathbf{H}_i^{th})^2 \rangle = \gamma^2 \delta t$$

since the thermodynamic average is taken for a finite duration. The random numbers from the Box–Muller algorithm thus have to be multiplied by a factor $\gamma = \sqrt{\frac{2\alpha k_B T}{\delta t}}$. This means that, in practice, we may increase the time step δt if we decrease the Langevin term. The limit is that the timescale of the random field fluctuations should be shorter than that of the dynamics, so that the time step should be significantly shorter than, for example, the shortest vibrational period, as is customary in dynamics simulations.

Each time step, however, requires, in Heun's algorithm, two evaluations of the field, including the random contribution: one must use the same random numbers for both evaluations, as using two different sets would result in partial averaging out the fluctuations. The simulation of temperature effects would thus be wrong with consequences immediately be visible in, for instance, the transition temperature.

Finally, although [22] tends to oppose rotational matrix type algorithms and higher-order schemes such as Runge–Kutta (implicitly in a direct type integration), we show that one may very well use higher-order methods (here Heun) with the rotational matrix combining the advantages of both.
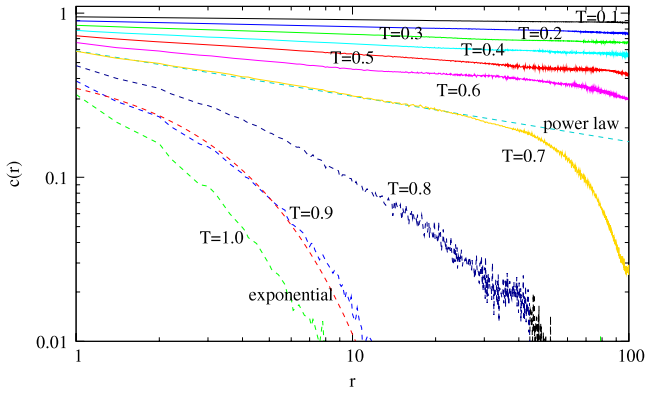
Figure 1. In-plane orientational correlation function (equation (8)) for a 128×128 sample, $0.1 \leqslant T \leqslant 1.0$ and $d = 0$. Scales are logarithmic so that power laws appear as straight lines. The power law $a\,r^\eta$ was fitted to the $T = 0.7$ line with $a = 0.59$ and $\eta = -0.277$ and the exponential law $A\,\mathrm{e}^{-\frac{r}{\xi}}$ was fitted to the $T = 0.9$ curve with $A = 0.51$ and $\xi = 2.61$.

3. Validation

The method was checked for cases for which the results are known, namely without dipolar interactions ($d = 0$). A Kosterlitz–Thouless phase transition, in which the in-plane magnetization vanishes, is expected at $T = 0.700(5)$ [25]. For $J_z = 0$, the magnon dispersion function in an infinite system [26] is $\omega = 4J|\sin\frac{q}{2}|$ for $T = 0$ with wavevector $\mathbf{q}$ in the x or y direction [27]: the shortest period is therefore expected at $\tau \sim \frac{2\pi}{\omega_0} \sim 1.57$. An integration time step δt of 0.02 is thus adequate. The damping was chosen as $\alpha = 0.0005$. The sample is a 64×64 square lattice in the (x, y) plane with free boundary conditions.

Both during the validation procedure and later, the initial conditions were chosen as a highly disordered configuration; then, for each set of parameters (T, α, d), one or several stabilization pre-runs were performed until the energy of the system was well stabilized: simulations with different histories, i.e. different stabilization sequences and dampings, were tested to yield the same results. Energy fluctuations about the average were checked to be symmetric. Finally a production run was done with the same parameters in order to compute dispersion curves, vortex trajectories and other quantities of interest in a stable sample. The final state of the production run was compared with its initial state. Computation was done on a cluster of computers allowing for the testing of a number of parameter sets simultaneously.

3.1. Magnetization

The in-plane magnetization

$$M^{\|} = \left(\frac{1}{n} \sum_\ell (s_{x_\ell}^2 + s_{y_\ell}^2) \right)^{\frac{1}{2}}$$

where s_{x_ℓ} and s_{y_ℓ} are the x and y components of spin ℓ, decreases from ± 1 for $T = 0$ to almost 0 for $T = 1$, with a steeper slope close to $T = 0.7$. For a $128 \times$ sample,

Table 1. Exponent η of the power law fitted to $c(r)$ (equation (8) and figure 1) as a function of temperature for $T \leqslant 0.7$. The values obtained close to the transition temperature are to be taken with caution as they depend rather strongly on the r range chosen for the fit (see, e.g., $T = 0.7$ in figure 1). Reference [25] (table III) gives $\eta = -0.160$ for $T = 0.6$ and -0.248 for $T = 0.7$. The function $\eta_0 \exp \frac{T}{T_0}$ was fitted to the data of this table, yielding parameters $\eta_0 = -0.013 \pm 0.002$ and $T_0 = 0.23 \pm 0.02$. Parameter η_0 can be understood as $\eta\,(T = 0)$, whereas T_0 sets the relevant temperature scale.

T	0.1	0.2	0.3	0.4	0.5	0.6	0.7
η	−0.018	−0.034	−0.058	−0.078	−0.112	−0.151	−0.277

the transition shows better: the smoothing of the expected Kosterlitz–Thouless transition is a finite-size effect.

According to the Mermin–Wagner theorem the in-plane magnetization should vanish in the thermodynamic limit, because the magnons destroy all long-range correlations in a 2D system with a continuous symmetry. However, our sample is too small for this to be seen directly, hence the non-zero magnetization. Indeed, the Kosterlitz–Thouless transition is characterized by a change in the decay of the orientational correlations: a power law ar^η below transition temperature and an exponential law $A\,\mathrm{e}^{-\frac{r}{\xi}}$ above. We have thus computed (in the larger 128×128 sample) the in-plane orientational correlation function:

$$c(r) = \frac{1}{m(r)} \sum_{i,j,\,|\mathbf{r}_{ij}|=r} \mathbf{s}_i^{\|} \cdot \mathbf{s}_j^{\|} \tag{8}$$

where $\mathbf{s}_i^{\|}$ is the in-plane component of spin i and $m(r)$ is the number of spin pairs at distance r. Figure 1 shows the result: the power law appears as straight lines with logarithmic scales for $T < T_c$; the decrease is much quicker above T_c (figure 1 plotted with a semi-log scale, instead of log–log here, yields an approximately straight line for $T > 0.7$ compatible with an exponential). One expects $\eta = -1/4$ at the transition temperature using periodic boundary conditions [25] and the fit in figure 1 yields -0.277 for $T = 0.7$; at lower temperatures the decay is even much weaker (table 1). The change in behavior occurs gradually as temperature increases: in figure 1, see, for example, $T = 0.7$ where the power law fits reasonably well only until $r \simeq 30$. For $T = 0.9$ the exponential fit is far from perfect with a reminiscence of a weaker decay for $r \simeq 10$. The $T = 0.8$ line shows an intermediate situation. This gradual change, instead of a sharp transition, is again a finite-size effect.

In any case, the very weak decay of the orientational correlations for $T < 0.7$ accounts for the apparent contradiction with the Mermin–Wagner theorem, especially for the smaller 64×64 sample for which such a weak decay is barely visible.

3.2. Elastic scattering

Although the system is of finite and relatively small size, in order to observe global structural properties and to make
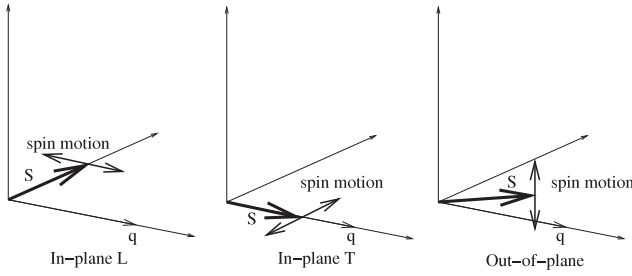
Figure 2. Polarization as seen by the three dynamic scattering functions (in this example, **q** is parallel to x: the expressions given in the text use the fact that the x and y axes are equivalent and add the corresponding terms). For the in-plane longitudinal, the spin is normal to the wavevector and spin motion parallel to it; for the transverse, the spin lies parallel to the wavevector and the motion is in-plane and normal to it; finally, for the out-of-plane, the spin orientation is unimportant but the motion is normal to the plane.

a connection with possible experiments, the usual static scattering functions can be computed:

$$|S_\gamma(\mathbf{q})|^2 = \left| \sum_\ell s_{\gamma_\ell} e^{i\mathbf{q}\cdot\mathbf{r}_\ell} \right|^2$$

where $\gamma = x$, y or z, **q** is the wavevector in the (x, y) plane, s_{x_ℓ}, s_{y_ℓ}, s_{z_ℓ} are the components of $\mathbf{s}_\ell$ and $\mathbf{r}_\ell$ their positions.

Without a dipolar term, for temperatures below the transition, the elastic scattering is simple: a strong central peak for the in-plane contributions is obtained and only noise for the out-of-plane contribution. Above the transition, the central peak disappears.

3.3. Dispersion curves

In order to simulate a so-to-say 'generic' inelastic scattering experiment and using elementary symmetry, three dynamic scattering functions were obtained: in-plane longitudinal (called L in the following) averaged over the equivalent $(1, 0)$ and $(0, 1)$ directions, in-plane transverse (T) averaged, and out-of-plane (Z), also averaged, i.e.

$$\text{(L)} \quad |S_{\rm L}(q, \omega)|^2 = \left| \int \sum_\ell (s_{x_\ell} e^{iqr_{x_\ell}} + s_{y_\ell} e^{iqr_{y_\ell}}) e^{i\omega t} \, dt \right|^2$$

$$\text{(T)} \quad |S_{\rm T}(q, \omega)|^2 = \left| \int \sum_\ell (s_{x_\ell} e^{iqr_{y_\ell}} + s_{y_\ell} e^{iqr_{x_\ell}}) e^{i\omega t} \, dt \right|^2$$

$$\text{(Z)} \quad |S_z(q, \omega)|^2 = \left| \int \sum_\ell (s_{z_\ell} e^{iqr_{x_\ell}} + s_{z_\ell} e^{iqr_{y_\ell}}) e^{i\omega t} \, dt \right|^2$$

where q is the (scalar) wavenumber, and r_{x_ℓ} and r_{y_ℓ} are the components of the spin positions. These three scattering functions are, of course, not independent as $s_{x_\ell}^2 + s_{y_\ell}^2 + s_{z_\ell}^2 = 1$.

Since most of the spins lie mainly in-plane, $S_{\rm L}(q, \omega)$ is essentially sensitive to the motion of spins lying perpendicularly to the wavevector and oscillating about the vertical axis; $S_{\rm T}(q, \omega)$ is sensitive to the motion of spins lying parallel to the wavevector and also oscillating about the z axis, whereas $S_z(q, \omega)$ sees spins that oscillate about a horizontal axis (figure 2).

Figure 3 shows the L dispersion curve for $T = 0.1$ in the ordered phase: the zone-boundary frequency is slightly below $\omega = 4$, as should be expected; this frequency decreases as temperature increases. A lower-frequency branch also shows, near the zone boundary, more clearly in the out-of-plane Z curve; this branch can be attributed to 'surface' modes, for which the spins have fewer neighbors, and therefore weaker coupling and lower frequency.

We may now introduce dipolar interactions and analyze results with the same methods. In this paper, we restrict our analysis to the case $d = 0.2$, a value chosen large enough for the dipolar interactions to show clearly.

4. Results with dipolar interactions

4.1. Structure for $d = 0.2$

4.1.1. Snapshots and correlations in real space. We first show several configurations for $d = 0.2$ and $T \in [0.1, 1]$ (figure 4) after relaxation. These snapshots, taken at different temperatures, show a central vortex at low temperatures.

The central vortex configuration is quite standard; however, in most cases it is accompanied by an out-of-plane magnetization component at the core of the vortex (both through simulations, e.g. [18], and experiments, e.g. [28]) which is absent in our case. While the vortex configuration
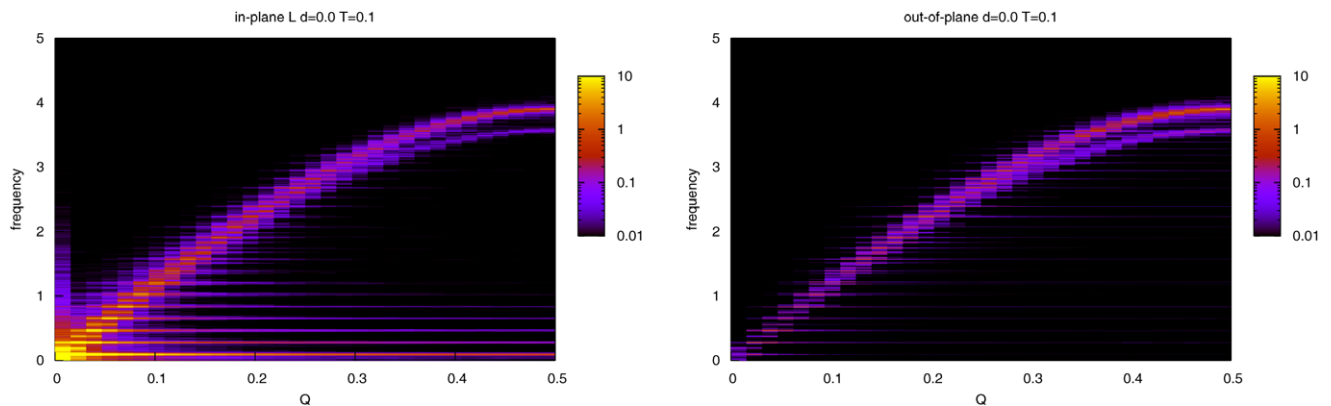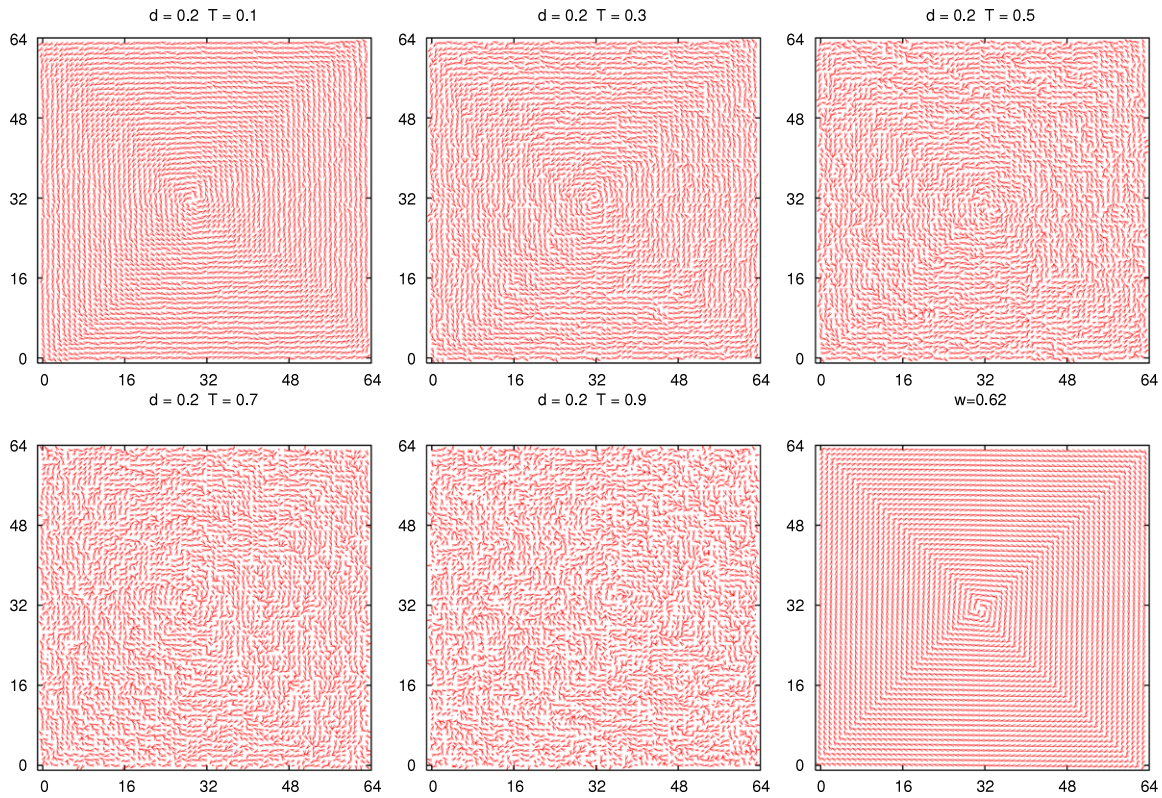

Figure 3. In-plane longitudinal (left) and out-of-plane (right) dispersion curves for $d = 0$ and $T = 0.1$. The q units are reduced, i.e. the Brillouin zone boundary is at $q = 0.5$, not π/a. Note that the intensity color scale is logarithmic.

Figure 4. In-plane configurations for $d = 0.2$ and increasing temperature. A central vortex is visible at low temperatures and disappears when $T \sim 0.7$. Bottom right: model for orientational correlation function with $w = 0.62$ (see text, section 4.1.1).

is energetically favorable for the dipole–dipole interaction because of the closed loops it involves, it is energetically costly for the Heisenberg interaction because of the large spin–spin angles at the vortex core. In an isotropic Heisenberg model, with $J_z = 1$, the cost of a vortex can be partially compensated for by out-of-plane spin orientations that will effectively reduce spin–spin angles, but in the anisotropic X–Y model with $J_z = 0$, the out-of-plane orientations are also energetically costly and do not occur, at least for $d = 0.2$.

The central vortex disappears when temperature increases above approximately $T = 0.7$. For $T = 0.1$, the fourfold symmetry of the sample plays a visible role, as the spins tend to lie parallel to each side of the square with a relatively sharp orientation change on each diagonal, whereas for, say, $T = 0.5$, this is not as clear although the central vortex remains distinguishable. However, 'processionary caterpillar'-like configurations in which the spins tend to sit in sinuous lines remain even at high temperature, the lines becoming more tormented and shorter with increasing temperature.

The corresponding in-plane orientational correlation functions are shown in figure 5. For distances larger than half of the size of the sample, the correlation function is negative which is consistent with figure 4. This feature decreases rapidly for $T > 0.7$: there is a visible gap between the $T = 0.7$ (yellow line pointed at by the $T = 0.7$ arrow in figure 5) and the $T = 0.8$ lines (black dashed line) for $r \sim 64$. The apparently peculiar behavior for $T = 0.2$ (blue line) will be discussed with figure 12 in section 4.2.2.

If one considers the $T = 0.1$ configuration of figure 4, one may, as a first crude representation, divide the square sample

into four equal sectors in which the spins are parallel to each other and to the closest edge of the square, whereas spins from neighboring sectors are orthogonal. However, the transitions from one sector to another should not be sharp, so we must superimpose on this structure a continuous rotation of spins about the middle of the sample, i.e.

$$\mathbf{s}(\mathbf{r}) = \mathbf{e}_z \times \frac{\mathbf{r}}{|\mathbf{r}|}.$$

So, if we give weight w to the rotation and $1 - w$ to the four-sector model, we obtain a configuration of which the orientational correlation function may be computed in the same way as for figure 5: the results are compared in figure 6 with weight $w = 0.62$ ($w = 0$ yields a straight line: $c(r) = 1 - 2r/l$, where l is the size of the sample, 64 here. Increasing w increases the double curvature).

This description is reasonably adequate for low temperatures but, as temperature increases, the sinuosity of the caterpillar lines increases and induces an additional short-range decay of the correlation function (see $T = 0.8$, 0.9 and 1.0 for $r < 8$ in figure 5).

4.1.2. Elastic scattering. A typical elastic scattering $|S_x(\mathbf{q})|^2$ is shown in figure 7. $|S_x(\mathbf{q} = 0)|^2$ naturally vanishes as the overall magnetization $M_x = \sum_\ell S_{x,\ell}$ vanishes because of symmetry. The two peaks should be situated at $\delta_q = \frac{2\pi}{32} \simeq 0.2$ from the center which seems to be the case, given the resolution of the figure which is also δ_q, set by the size of the sample. $|S_y(\mathbf{q})|^2$ is quite similar, whereas $|S_z(\mathbf{q})|^2$ only shows noise,
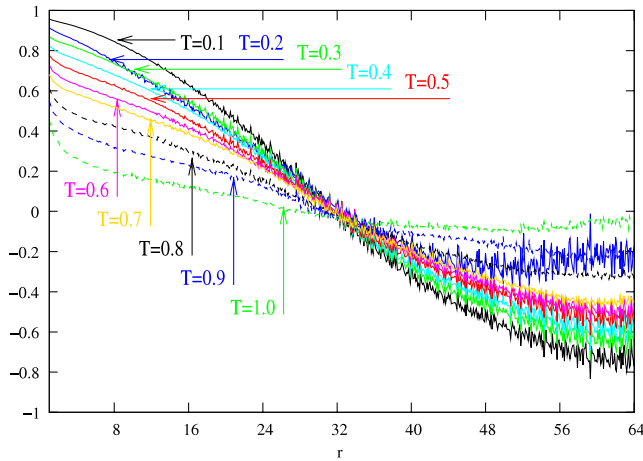
Figure 5. In-plane orientational correlation function $c(r)$ (equation (8)) for $d = 0.2$ and for temperatures $T \in [0.1, 1]$.
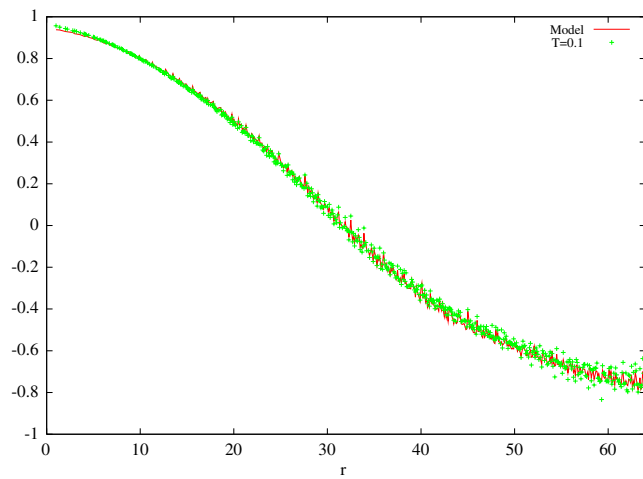

Figure 6. In-plane orientational correlation function for $d = 0.2$ and for temperatures $T = 0.1$ (green points) and model for $w = 0.62$ (red line). (see text, section 4.1.1).

so no out-of-plane structure is observed as pointed out in section 4.1.1.

4.2. Dynamics for $d = 0.2$

4.2.1. Dispersion curves.
Figure 8 shows the dispersion curves for $d = 0.2$ and $T = 0.1$.

The in-plane longitudinal curve corresponds to an exploration in reciprocal space along the q_x axis of figure 7, whereas the transverse is along the q_y axis.

Several differences with the Heisenberg model without dipolar interaction can be noted.

(i) For $q = 0$ the frequency does not decrease to zero. Clearly, a uniform rotation of all spins will not change the Heisenberg interaction, hence the usual zero-frequency mode in that case (figure 3), but the dipolar term does change, thus giving a frequency gap. This is consistent with the absence of a central peak in figure 7.
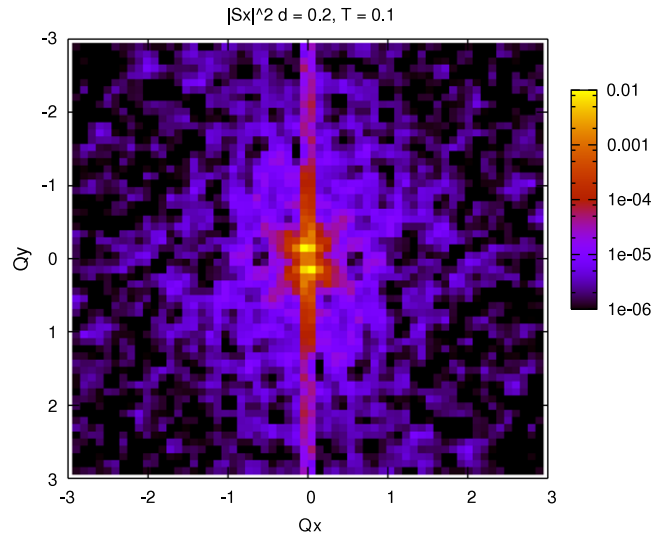

Figure 7. Elastic scattering function $|S_x(\mathbf{q})|^2$ for $d = 0.2$ and $T = 0.1$. The intensity color scale is logarithmic.

(ii) The above observation could be questioned for the transverse mode: however, the elastic peaks along q_y in figure 7 are intrinsically very close to the zone center, and clearly orders of magnitude stronger than inelastic peaks: some spilling into the inelastic scattering function is therefore to be expected.

(iii) Unsurprisingly, the zone-boundary frequency is higher than in the pure Heisenberg model.

(iv) The transverse mode is at lower frequencies than the longitudinal one.

The low-frequency Brillouin zone center of the dispersion curve shows some structure (figure 9) but the main effect of temperature is to increase intensity in the zone-center frequency gap: this can be connected to the vortex motion (see section 4.3.1).

4.2.2. Vortices.
We have computed vortex positions with time: this can be done by obtaining orientations φ_i of the four spins that surround a given unit cell of the lattice (figures 10 and 11) and computing $\delta\varphi_i = \varphi_{i+1} - \varphi_i$, $\delta\varphi_i \in [-\pi, \pi]$, $i \in [1, 4]$. The sum $\varphi_t = \sum_{i=1}^{4} \delta\varphi_i$ yields the overall rotation about the square: if that rotation is equal to 2π, a vortex is detected on that square, while if it is equal to -2π, then it is an anti-vortex; otherwise $\varphi_t = 0$. If a vortex or an anti-vortex is found, the (x, y) coordinates of the unit cell are then saved along with time, allowing for a 3D plot (figure 12) to follow vortex trajectories with time.

The lowest temperature graph ($T = 0.1$) confirms the central vortex structure, but also shows that this vortex undergoes some motion. $T = 0.2$ and 0.3 show a two-vortex structure (vortex and anti-vortex): however, the $T = 0.3$ graph shows the collapse of a lateral vortex–anti-vortex pair (the vortex—in green—is partially visible behind the central vortex—also green—while the anti-vortex is red). This means that the single central vortex structure seems to be stable but that a small number of vortices can remain a relatively long
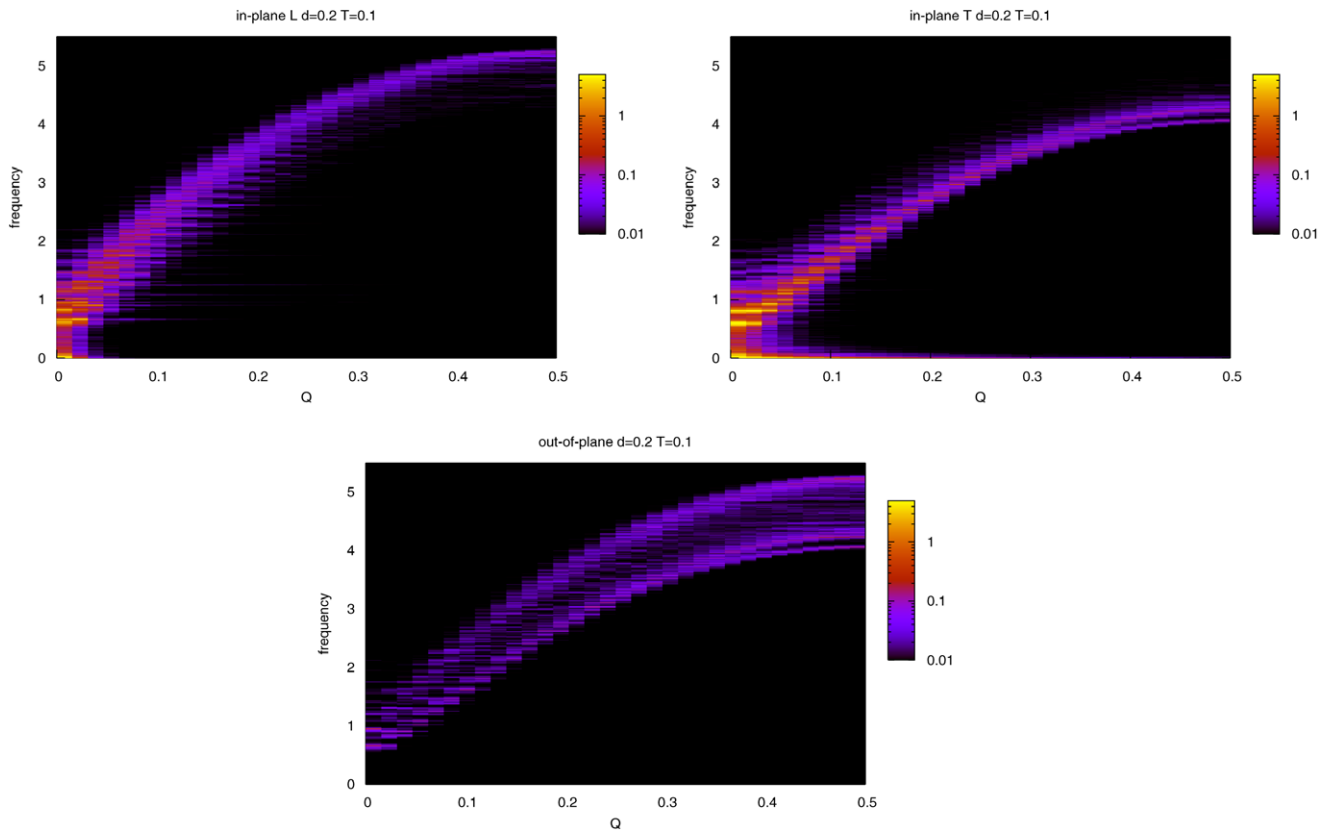
Figure 8. Dispersion curves for $d = 0.2$ and $T = 0.1$. In-plane longitudinal (left), in-plane transverse (right) and out-of-plane (bottom). Logarithmic color scale.
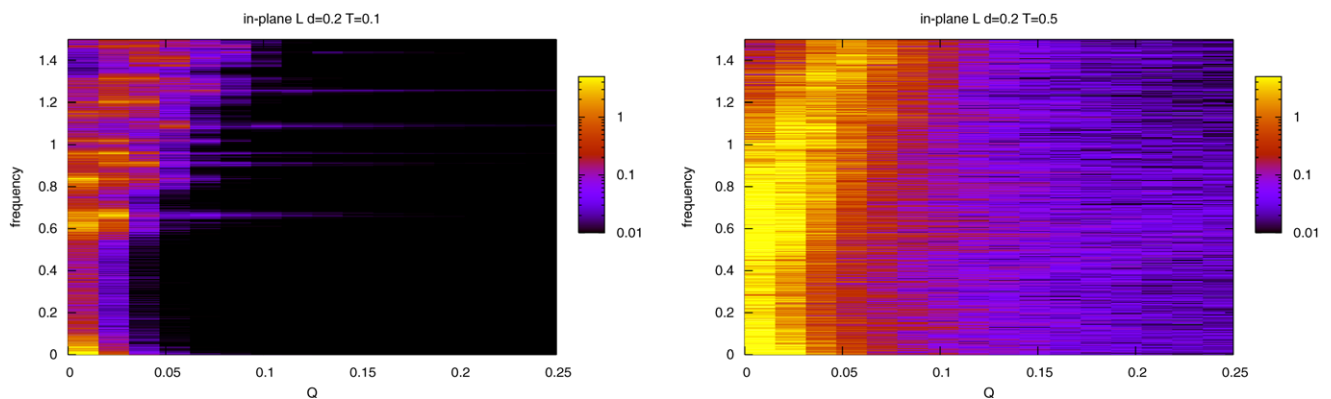

Figure 9. Effect of temperature on the low-frequency Brillouin zone-center part of the in-plane longitudinal dispersion curve. $T = 0.1$ (left) and $T = 0.5$ (right).

time before disappearing with a small energy gain (from -4.19 to -4.20 in that specific case, not significantly above thermal fluctuations despite the fact that they are not close to each other). This also explains the odd behavior of the $T = 0.2$ orientational correlation function in figure 5. The energy cost of a vortex–anti-vortex pair in addition to the central vortex is thus weak. The creation of such a pair is also relatively easy, as can be observed at slightly higher temperatures ($T = 0.5$ and 0.6). Above $T = 0.7$, the vortex density increases rapidly.

Table 2 gives a count of the detected vortices averaged over time: non-integers mean that vortices do not always last

for the entire simulation. The difference in numbers between vortices and anti-vortices is usually one, meaning we have pairs in addition to a central vortex (the exception being $T = 0.2$ with a single pair): at higher temperatures this could not be seen in figure 12 because of the high density of vortices cluttering the graph: however, the central vortex does seem to remain. Again, the sharp increase of the number of vortices above $T = 0.7$ can be noted: however, it is compatible with a simple thermally activated process as described by an Arrhenius law.
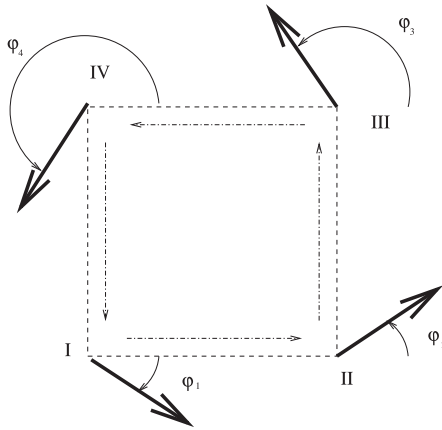
Figure 10. Vortex search procedure: one explores, for instance counter-clockwise, the orientations of the four spins that surround a unit cell of the square lattice and computes the angular differences $\varphi_{i+1} - \varphi_i$ of two consecutive spins. The sum of these differences should be equal to zero except if a complete rotation was performed: if it is equal to 2π a vortex is detected, while if it is -2π, then it is an anti-vortex.
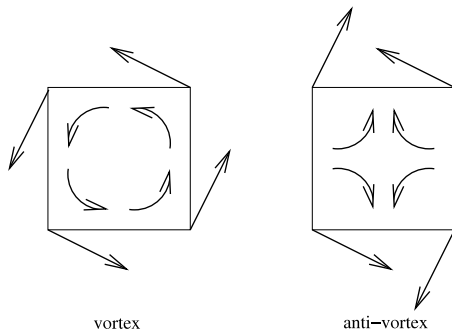

Figure 11. Examples of a vortex and an anti-vortex as obtained from the procedure shown in figure 10. The curved arrows give an idea of what they look like from a distance.

4.3. Vortex motion

4.3.1. On thermalized configurations. Figure 12 shows that the central vortex undergoes motion and that vortex–anti-vortex pairs are created and annihilated with time. The lifetime of these pairs is short with respect to the timescale of the figure. The central vortex moves randomly, but never far from the middle of the sample. This motion is relatively slow but does not display much structure in the frequency domain. It shows in the dispersion curve (figure 9) as a strong increase with temperature of the low-frequency Brillouin zone-center part of the dispersion curve. The out-of-plane dispersion curve (figure 13) is not sensitive to this effect since the vortex motion is mainly in-plane: this supports our interpretation. The effect of temperature is thus not so much to change the dynamics of the spin system (although the slope of the dispersion curve does change slightly) but to increase the number of vortices and therefore to enhance the low-frequency long-range motion.

In figure 9 (left), frequency 0.6 for $q \sim 0$ is the frequency associated with overall rotation of all spins in the sample, assuming that the motion of the central vortex can be neglected

Table 2. Vortex and anti-vortex count for $d = 0.2$: number of vortices counted for each temperature (figure 12) and averaged over time. A comparison with an Arrhenius law is given on the last line.

T	0.1	0.2	0.3	0.4	0.5	0.6	0.7	0.8	0.9	1.0
Vortices	1	1	1.16	1	1.09	1.69	4.4	14.7	36.8	96.3
Anti-vortices	0	1	0.16	0	0.09	0.69	3.4	13.8	35.8	95.2
$10^5 e^{-7/T}$					0.08	0.86	4.5	15.8	41.9	91.2

as a first approximation. Now, temperature excites modes at lower frequencies which can be understood as spin rotations connected with the small energies involved with vortex–anti-vortex creation and annihilation processes: this involves a rearrangement of a relatively large number of spins and can hardly be considered as a local effect, hence its manifestation mainly in the neighborhood of the Brillouin zone center.

The time Fourier transform of the distance of a vortex from the middle of the sample was computed for $d = 0.2$ and $T = 0.1$ (in a single-vortex configuration as in figure 12) and the corresponding spectral intensity plotted against frequency (figure 14). For $\omega > \omega_{th} = 10^{-2}$ the decay is a power law $a\omega^p$ with exponent $p = -2$, meaning the motion is a standard memoryless drunkard's walk. For lower frequencies, the decay is slower, with an exponent approximately $q \in [-0.2, 0]$. The threshold frequency $\omega_{th} = 10^{-2}$ yields a characteristic time of about 100 time units.

4.3.2. 'Custom-made' initial configurations and relaxation. All previous results were obtained from arbitrary and highly disordered configurations which were stabilized at a given temperature, the relaxation process itself being ignored. Indeed, we can expect the single central vortex structure to be the equilibrium configuration, because firstly the dipolar interaction favors structures in which the spins tend to form loops, and secondly the free boundary conditions favor situations in which the spins at the edge remain parallel to the edge. However, figure 12 shows situations which are different, for which this relaxation process may be questioned (e.g. $T = 0.2$ and 0.3). One may then prepare 'custom-made', ideal, initial configurations and observe the relaxation itself through vortex trajectories.

Figure 15 shows a two-vortex initial configuration. Relaxation was performed at relatively low temperature ($T = 0.1$) in order to prevent perturbations by vortex–anti-vortex creations and annihilations. One observes that the vortices move away from each other with an effective repulsive interaction: the leftmost vortex first moves to the left and then back towards the middle, while the other vortex is expelled from the sample. The first vortex then gradually settles in the middle of the sample with a characteristic time of approximately 200 time units, which is of the same order of magnitude of the inverse of the threshold frequency ω_{th} obtained in the previous section from figure 14.

Figure 16 shows the same with a vortex–anti-vortex pair: this configuration seems quite stable as already could be inferred from figure 12, $T = 0.2$, with no tendency to expel either the vortex or the anti-vortex: the additional information here, due to better time resolution, is that the vortex tends
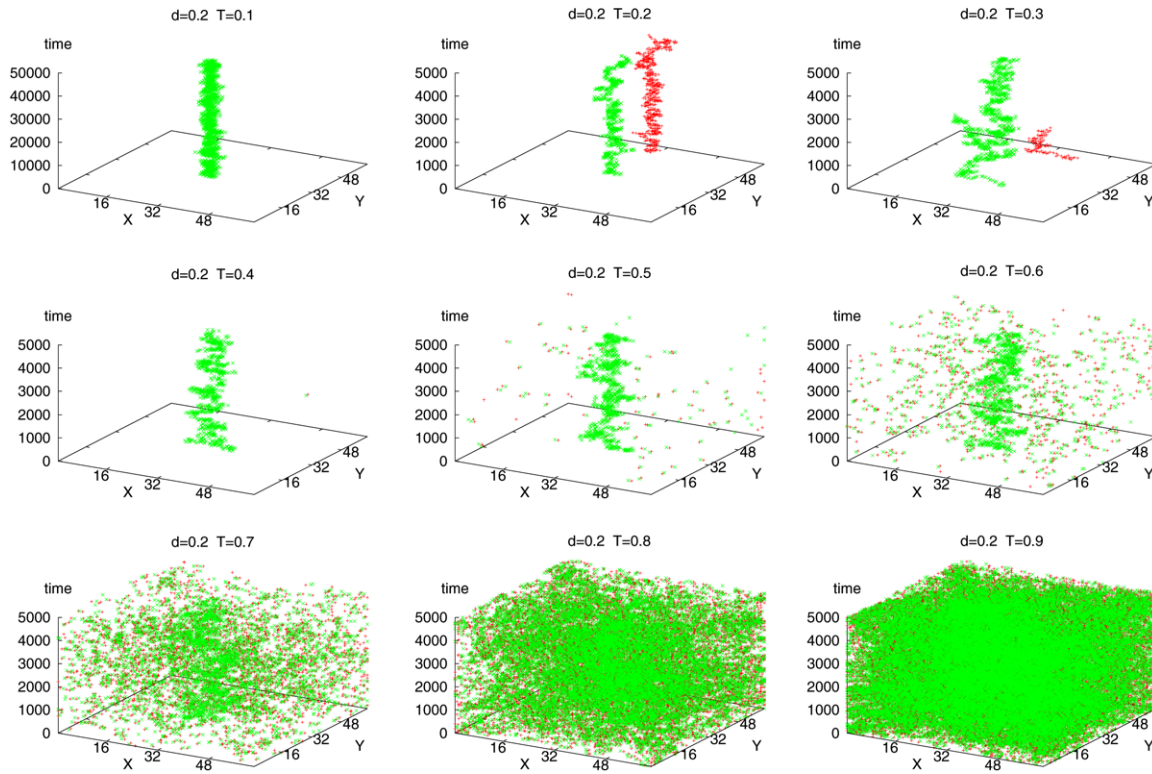
Figure 12. Vortices for $d = 0.2$ and increasing temperature. Time axis is vertical, the two others being the instantaneous positions of detected vortices (green, or grey in print) and anti-vortices (red, or black in print). Note that the timescale is different on the top left graph ($T = 0.1$).
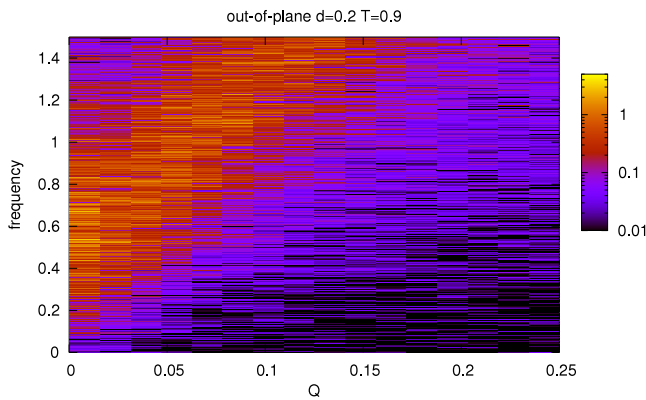

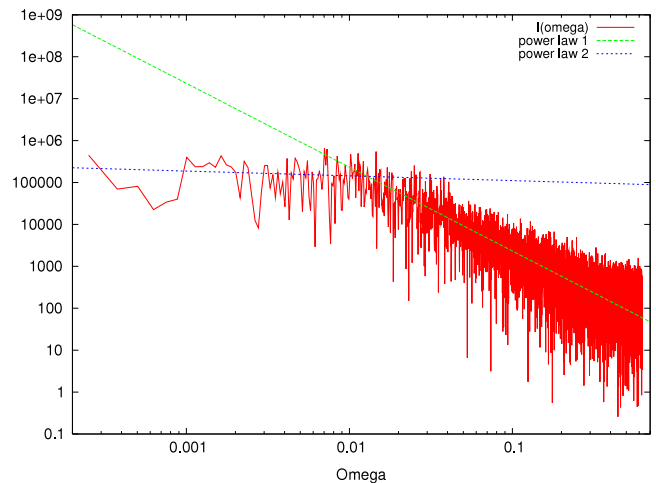**Figure 13.** Low-frequency Brillouin zone-center part of the out-of-plane dispersion curve for $T = 0.9$.

Figure 14. Spectral intensity of the distance of a vortex from the center of the sample for $d = 0.2$ and $T = 0.1$. The straight lines on the log–log plot correspond to power laws. Power law 1 (green dashed line) $a\omega^p$ was fitted for $\omega > 0.01$ and power law 2 (blue dots) $b\omega^q$ for $\omega < 0.01$. The fits yield $a = 23.2$, $p = -2$, $b = 85 \times 10^3$ and $q = -0.1$, the standard error however being 90% for q.

to settle in the middle of the sample, whereas the anti-vortex moves to the side, although the initial configuration had them both at an equal distance from the center.

An interesting process is shown in figure 17 in which the initial configuration has two vortices and two anti-vortices. A vortex and an anti-vortex merge and annihilate rapidly while the two remaining relax towards a situation in which the vortex lies in the middle of the sample and the anti-vortex closer to the edge as in figure 16. This also shows the capability of vortices to move around the sample quite a lot in order to seek some equilibrium configuration.

Now the single-vortex situation shown in figure 12 for $T = 0.1$ yields an average energy of $E = -4.628$ with a standard deviation $\sigma = 0.003$. The vortex–anti-vortex pair configurations of figures 16 and 17 have energies of -4.60 or -4.61. This means that, since the energy difference is significantly larger than the standard deviation, the single-
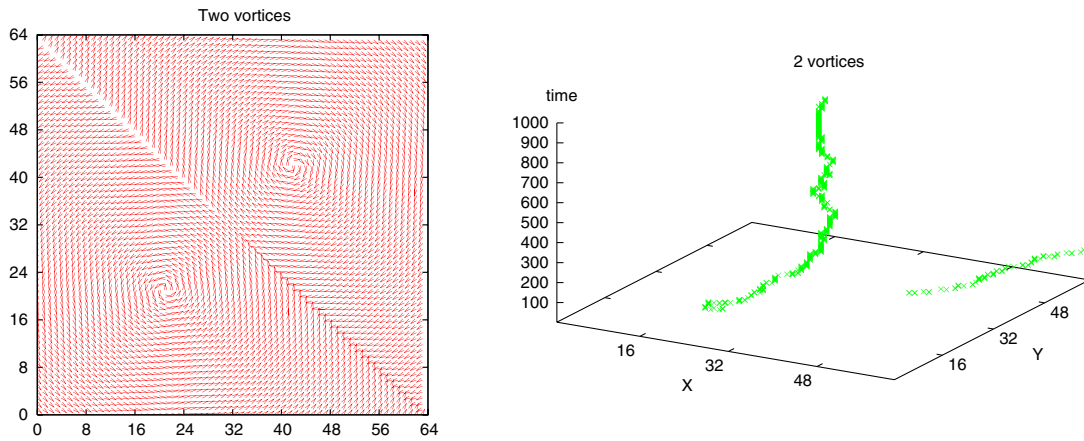
Figure 15. 'Custom-made' initial configuration with two vortices with opposite chiralities (left) and vortex trajectories during relaxation at $T = 0.1$ (right). One vortex is expelled while the other migrates to the middle of the cluster.
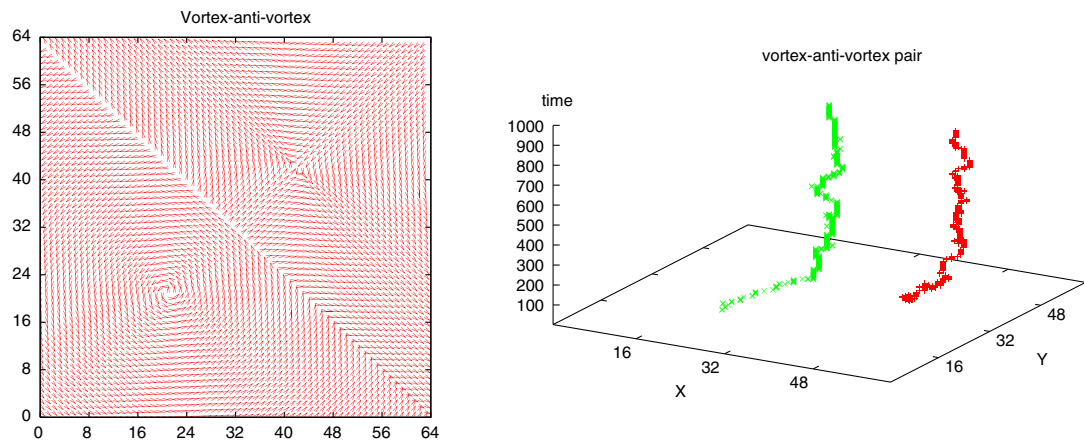

Figure 16. Initial configuration with a vortex–anti-vortex pair (left), and trajectories during relaxation at $T = 0.1$ (right); the vortex is in green, the anti-vortex in red.
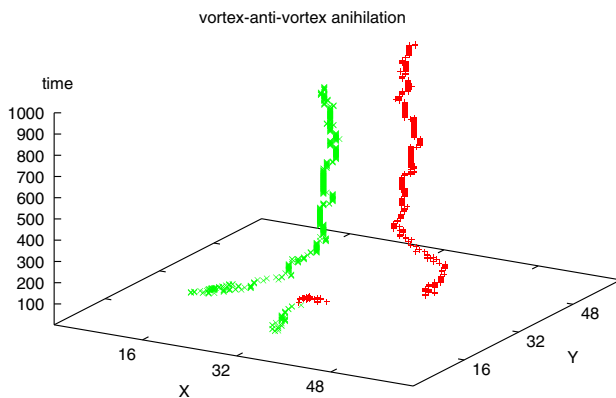

Figure 17. Vortex–anti-vortex annihilation followed by the relaxation of the remaining vortices.

vortex configuration is clearly more stable, but this difference is small ($\sim 5\sigma$) and we can therefore expect, as in figure 12, other configurations to remain even after a long stabilization period.

5. Conclusion

We have replaced the straightforward integration of the Landau–Lifshitz equation, which does not ensure spin length conservation, with an explicit precession about the local field, which does. This method was tested to produce the expected Kosterlitz–Thouless transition with the correct orientational correlation functions for the XY-Heisenberg model. Aside from being intellectually more satisfying, explicit precession allows reliable simulations without artificial corrections.

With dipole–dipole interactions, the structure and dynamics, including vortex dynamics, of these spin systems could then be thoroughly studied. The most frequently observed structure for $d = 0.2$ and $T \in [0.1, 0.7]$ is that of a single central vortex with an overall rotation of spin orientations about that central vortex. No structured out-of-plane component was observed because of the anisotropy of the XY-Heisenberg model. Vortex–anti-vortex pairs are metastable with a small increase of energy and their number increases with temperature following an Arrhenius law. The low temperature in-plane orientational correlation functions are compatible with an overall rotation of the spins about the central vortex and

roughly parallel to the sample edges; at higher temperatures the long-range correlations disappear with a jump for $T \simeq 0.7$.

Dispersion curves were obtained showing the appearance of a frequency gap at the zone center in all symmetries, the transverse mode being lower in frequency than the longitudinal: this shows clearly in the out-of-plane symmetry in which both curves are visible.

The low-frequency, low-wavenumber dynamics as seen in the dispersion curves is an indication that motion either of the vortices themselves or of the inter-vortex domains is present. Vortex motion could also be observed: 'fast' motion is essentially of random-walk type, while 'slow' motion shows a mainly flat spectral intensity, consistent with the fact that a stable vortex remains at the center of the sample with quick random motion in the center's vicinity. Relaxation processes from chosen ideal situations were obtained: the single central vortex structure arises spontaneously while two-vortex situations are unstable, one of the vortices being expelled. Vortex–anti-vortex annihilation could be observed.

Acknowledgments

References

[1] Cowburn R P 2002 *J. Magn. Mater.* **242–245** 505
[2] Kawaji J, Kitaizumi F, Oikawa H, Niva D, Homma T and Osakaf T 2005 *J. Magn. Magn. Mater.* **287** 245
[3] Raabe J, Pulwey R, Sattler R, Schweiboeck T, Zweck J and Weiss D 2000 *J. Appl. Phys.* **88** 4437
[4] Schneider M, Hoffmann H, Otto S, Haug T and Zweck J 2002 *J. Appl. Phys.* **92** 1477
[5] Fernandez A and Cerjan C J 2000 *J. Appl. Phys.* **87** 1395
[6] Pokhil T, Song D and Nowak J 2000 *J. Appl. Phys.* **87** 6319
[7] Demokritov S O, Hillebrands B and Slavin A N 2001 *Phys. Rep.* **348** 441
[8] Hillebrands B and Ounadjela K (ed) 2002 *Spin Dynamics in Confined Magnetic Structures* (*Topics in Applied Physics* vol 83) (Berlin: Springer)
[9] Park J P, Eames P, Engebretson D M, Berezovky J and Crowell P A 2003 *Phys. Rev.* B **67** 020403(R)
[10] Buess M, Höllinger R, Haug T, Perlzmaier K, Krey U, Pescia D, Scheinfein M R, Weiss D and Back C H 2004 *Phys. Rev. Lett.* **93** 077207
[11] Choe B, Acremann Y, Scholl A, Bauer A, Doran A, Stöhr J and Padmore H A 2004 *Science* **304** 420
[12] Rohart S, Tejeda A, Ohresser P, Scheurer F, Bencock P, Ferr J and Rousset S 2006 *Phys. Rev.* B **73** 165412
[13] Kim D-H, Jeong J-R, Cho Y-C and Shin S-C 2005 *J. Magn. Magn. Mater.* **286** 23
[14] Kamppeter T, Mertens F G, Moro E, Sanchez A and Bishop A R 1999 *Phys. Rev.* B **59** 11349
[15] Vedmedenko E Y, Oepen H P, Ghazali A, Lévy J-C S and Kirschner J 2000 *Phys. Rev. Lett.* **84** 5884
[16] Weis J J 2003 *J. Phys.: Condens. Matter* **15** S1471
[17] Nowak U 2001 *Annual Reviews of Computational Physics IX* ed D Stauffer (Singapore: World Scientific) p 105
[18] Wieser R, Usadel K D and Nowak U 2006 *Phys. Rev.* B **74** 094410
[19] Kosterlitz J M and Thouless J D 1973 *J. Phys. C: Solid State Phys.* **6** 1181–203
[20] Kosterlitz J M 1974 *J. Phys. C: Solid State Phys.* **7** 1146–60
[21] Weisstein E W *et al* 2009 *MathWorld* http://mathworld.wolfram.com/RodriguesRotationFormula.html
[22] Visscher P B and Feng X 2002 *Phys. Rev.* B **65** 104412
[23] Chubykalo O, Hannay J D, Wongsam M, Chantrell R W and Gonzales J M 2002 *Phys. Rev.* B **65** 184428
[24] Press W H, Teukolsky S A, Vettering W T and Flannery B P 1992 *Numerical Recipes* (Cambridge: Cambridge University Press)
[25] Cuccoli A, Tognetti V and Vaia R 1995 *Phys. Rev.* B **52** 10221
[26] Evertz H G and Landau D P 1996 *Phys. Rev.* B **54** 12302
[27] Mertens F G, Bishop A R, Wysin G M and Kawabata C 1989 *Phys. Rev.* B **39** 591
[28] Bolte M, Meier G, Krüger B, Drews A, Eiselt R, Bocklage L, Bohlens S, Tyliszczak T, Vansteenkiste A, Van Waeyenberge B, Chou K W, Puzic A and Stoll H 2008 *Phys. Rev. Lett.* **100** 176601